

# Soft and Hard X-Ray Emissions from the Anomalous X-ray Pulsar 4U 0142+61 Observed with Suzaku

T. Enoto<sup>1,2</sup>, K. Makishima<sup>1,3</sup>, K. Nakazawa<sup>1</sup>,  
M. Kokubun<sup>4</sup>, M. Kawaharada<sup>4</sup>, J. Kotoku<sup>5</sup>, and N. Shibazaki<sup>6</sup>  
*enoto@stanford.edu*

<sup>1</sup> *Department of Physics, The University of Tokyo, 7-3-1 Hongo,  
Bunkyo-ku, Tokyo 113-0033, Japan*

<sup>2</sup> *Current address: Kavli Institute for Particle Astrophysics and Cosmology,  
Department of Physics and SLAC National Accelerator Laboratory,  
Stanford University, Stanford, CA 94305, USA*

<sup>3</sup> *High Energy Astrophysics Laboratory, Institute of Physical and Chemical Research (RIKEN),  
Wako, Saitama 351-0198, Japan*

<sup>4</sup> *Institute of Space and Astronautical Science (ISAS), Japan Aerospace Exploration Agency (JAXA),  
3-1-1 Yoshinodai, Chuo-ku, Sagami-hara, Kanagawa 252-5210, Japan*

<sup>5</sup> *Department of Radiological Technology, Faculty of Medical Technology, Teikyo University  
2-11-1 Kaga, Itabashi-ku, Tokyo 173-8605, Japan*

<sup>6</sup> *Department of Physics, Faculty of Science, Rikkyo University,  
3-34-1 Nishi-Ikebukuro, Toshima-ku, Tokyo 171-8501, Japan*

(Received ; accepted )

## Abstract

The anomalous X-ray pulsar 4U 0142+61 was observed with Suzaku on 2007 August 15 for a net exposure of  $\sim 100$  ks, and was detected in a 0.4 to  $\sim 70$  keV energy band. The intrinsic pulse period was determined as  $8.68878 \pm 0.00005$  s, in agreement with an extrapolation from previous measurements. The broadband Suzaku spectra enabled a first simultaneous and accurate measurement of the soft and hard components of this object by a single satellite. The former can be reproduced by two blackbodies, or slightly better by a resonant cyclotron scattering model. The hard component can be approximated by a power-law of photon index  $\Gamma_h \sim 0.9$  when the soft component is represented by the resonant cyclotron scattering model, and its high-energy cutoff is constrained as  $> 180$  keV. Assuming an isotropic emission at a distance of 3.6 kpc, the unabsorbed 1–10 keV and 10–70 keV luminosities of the soft and hard components are calculated as  $2.8 \times 10^{35}$  erg s<sup>-1</sup> and  $6.8 \times 10^{34}$  erg s<sup>-1</sup>,

respectively. Their sum becomes  $\sim 10^3$  times as large as the estimated spin-down luminosity. On a time scale of 30 ks, the hard component exhibited evidence of variations either in its normalization or pulse shape.

**Key words:** magnetic fields — neutron stars: individual (4U 0142+61)— X-rays: general, individual (4U 0142+61)

## 1. Introduction

Anomalous X-ray pulsars (AXPs), comprising at present  $\sim 9$  objects discovered in the local universe, are characterized by rotational periods in the range  $P = 5 - 12$  s, and spin down rates as  $\dot{P} \sim 10^{-11}$  s s $^{-1}$ . Together with soft gamma repeaters (SGRs), AXPs are thought to form a subgroup of neutron stars called “magnetars”, of which the surface magnetic field strengths are believed to reach  $\sim 10^{14-15}$  G (Thompson & Duncan 1995; Thompson & Duncan 1996; Woods & Thompson 2006). In energies below  $\sim 10$  keV, AXPs exhibit spectra which are much softer than those of ordinary binary X-ray pulsars, while harder than those of isolated neutron stars. Their X-ray luminosities ( $10^{34-35}$  erg s $^{-1}$ ), which often exceed up to two order of magnitude those available from their spin-down power ( $\sim 10^{32}$  erg s $^{-1}$ ), are usually thought to be sustained by a release of energies stored in their ultra-strong magnetic fields (Duncan & Thompson 1992; Thompson & Duncan 1995).

A novel observational window onto magnetars has been opened by the INTEGRAL discoveries of a distinct pulsed hard X-ray component from at least 3 AXPs and 2 SGRs (Kuiper et al. 2004; Mereghetti et al. 2005; den Hartog et al. 2006; Kuiper et al. 2006; Götz et al. 2007). This component extends to  $\sim 100$  keV or more with a very flat photon index of  $\Gamma \sim 1$ , and exhibits a luminosity comparable to or higher than that in the softer X-ray band. Although theoretical accounts for this enigmatic component are far from settled (e.g., Heyl & Hernquist 2005; Beloborodov & Thompson 2007; Baring & Harding 2007), its near-absence in other types of X-ray sources suggests its close relation to the proposed strong magnetic fields of magnetars.

The study of magnetars now requires a broad energy band, because their soft and hard components, which are generally variable, must be measured simultaneously and accurately. This makes Suzaku (Mitsuda et al. 2007) an ideal observatory. In fact, the X-ray Imaging Spectrometer (XIS), operating in the 0.2–12 keV range (Koyama et al. 2007), provides high-quality data of their soft components. Simultaneously, the Hard X-ray Detector (HXD; Takahashi et al. 2007; Kokubun et al. 2007), consisting of HXD-PIN (10–70 keV) and HXD-GSO (40–600 keV), can conduct detailed spectroscopic studies of their hard components in considerably shorter exposures than are needed by INTEGRAL.

Such wide-band spectroscopic observations with Suzaku have allowed detections of the

hard-tail component from activated magnetars, including SGR 0501+4516 (Enoto et al. 2009; Rea et al. 2009; Enoto et al. 2010b) and 1E 1547.0-5408 (Enoto et al. 2010a). Through these observations, the hard X-ray emission from SGR 0501+4516 was revealed to form a component distinct from the soft X-rays, while the power-law-shaped hard-tail component of 1E 1547.0-5408 to extend to the soft X-ray band below 10 keV. Thus, a key point of the observation of magnetars is to detect and quantify their wide-band spectra simultaneously, without hampered by cross-calibration uncertainties or non-simultaneity involved in multi-satellite observations. This is a great advantage provided with Suzaku.

In the present paper, we report on a high sensitivity broadband observation of a prototypical magnetar 4U 0142+61 made with Suzaku. This object is one of the most luminous AXPs with  $P \sim 8.68$  s (Israel et al. 1994), located at the Galactic anti-center direction, probably on the Perseus arm (Durant & van Kerkwijk 2006a). Its pulsed hard X-ray emission was detected up to  $\sim 200$  keV by INTEGRAL and RXTE (Kuiper et al. 2006; den Hartog et al. 2006; den Hartog et al. 2008). On the other hand, past COMPTEL observations gave a flux upper limit in energies above 750 keV (Kuiper et al. 2006; den Hartog et al. 2006). If the source exhibits little time variations between these observations, the hard X-ray spectrum must turn over at energies between  $\sim 200$  and  $\sim 750$  keV, though it has not yet been clearly detected.

## 2. Observation and Data Reduction

We observed 4U 0142+61 with Suzaku from 04:04 UT on 2007 August 13 to 12:30 UT on August 15, for a gross duration of 203 ks and a net exposure of  $\sim 100$  ks. The XIS and the HXD were both operated in their normal modes, except that 1/4 window option was applied to the XIS to achieve a time resolution of 2 s.

We placed the source at the HXD nominal position, and adjusted the roll angle to avoid contaminating bright hard X-ray sources. In particular, we tried to minimize the confusion with the Be X-ray binary RX J0146.9+6121. Located  $24'$  off 4U 0142+61, this source exhibited a 20–50 keV flux comparable to that of 4U 0142+61 during INTEGRAL observations in 2003–2004 (den Hartog et al. 2006). As a result of the roll-angle adjustment, the HXD-PIN effective area onto RX J0146.9+6121 was  $\lesssim 29\%$  of that onto 4U 0142+61 in the 10–70 keV energy band. Based on this, and the reported steep spectrum ( $\Gamma \sim 3$ ; den Hartog et al. 2006), we regard the contamination of RX J0146.9+6121 to the HXD negligible. There were no other catalogued bright X-ray sources inside the HXD field of view.

We used the Suzaku data prepared via version 2.1 processing, and the HEASOFT version 6.4 or later tools. The employed data screening criteria were; (a) the time after an exit from the South Atlantic Anomaly should be  $>500$  s and  $>436$  s for the HXD and the XIS, respectively, while the time to the next entry should be  $>180$  s for the HXD. (b) the target should be above the Earth rim by  $>5^\circ$  for the HXD and the XIS, and, in case of the sunlit Earth rim, that should be  $>20^\circ$  for the XIS; (c) the instantaneous pointing direction should be within  $1'.5$  of the

mean; and (d) the geomagnetic cutoff rigidity should be  $>6$  GV. As a result of these screenings, we archived a net exposure of 99.7 ks with the XIS, and 94.7 ks with the HXD.

### 3. Data Analysis and Results

#### 3.1. Background subtraction

We accumulated the screened data of the XIS from a region within  $2'.0$  (2.8 mm) radius of the source centroid, and derived a background spectrum from another region which is symmetric with respect to the XIS field-of-view center. Corresponding `rmf` and `arf` files were created using `xisrmfgen` and `xissimarfgen` tools (Ishisaki et al. 2007), respectively.

The non-Xray background (NXB) of the HXD must be subtracted using appropriate models that emulate NXB events to be observed during the on-source exposure. Specifically, we utilized LCFITDT (`bgd_d 2.0 ver0804`) and LCFIT (`bgd_d 2.0 ver0804`) methods (Fukazawa et al. 2009) to create the fake NXB events of HXD-PIN and HXD-GSO, respectively. These fake photons were also screened by the same criteria as for the on-source event data.

Using the data acquired during Earth-occultation periods ( $\sim 20$  ks in total) in the present observation, we confirmed that the HXD-PIN and HXD-GSO spectra obtained therein can be reproduced by the employed NXB models both within  $\sim 1\%$ , which agrees with the typical uncertainties of these models. This calibration suggests that we are slightly ( $\sim 0.6\%$ ) under-subtracting the NXB of HXD-GSO. Thus, we finally subtracted the HXD-GSO background after increasing it by 0.6%, and include systematic uncertainties of 0.6% after Fukazawa et al. (2009).

#### 3.2. Source detection

Figure 1 shows background-subtracted light curves of XIS3 and HXD-PIN. For the soft X-ray light curve, we utilized the XIS3 data because those from XIS0 or XIS1 are more subject to artificial intensity variations synchronized with the orbital period of Suzaku, caused by thermal distortions of the spacecraft structure (Uchiyama et al. 2008). We do not show a light curve of HXD-GSO, since the NXB model for HXD-GSO is valid only for integrations longer than  $\sim 100$  ks for such low count rate objects. Thus, the source has been detected clearly not only by XIS3 but also by HXD-PIN, as the average HXD-PIN count rate,  $\sim 0.08$  c s $^{-1}$ , significantly exceeds the expected CXB rate of  $\sim 0.03$  c s $^{-1}$  (Kokubun et al. 2007).

At the binning as shown in Figure 1, the XIS3 count rate was constant during the observation within 15%. The possible variations seen in figure 1a can be mostly attributed to slight losses of signal photons, due to the thermal distortion of the spacecraft structure which caused the image outskirts to partially fall outside the 1/4 window. The HXD-PIN signals, with 550 s binning, are also roughly constant: the NXB-subtracted light curve can be fitted by a constant with  $\chi^2/\nu = 154.9/126$ . However, the HXD-PIN light curve may be slightly decreasing with time, because it can be fitted better ( $\chi^2/\nu = 142.2/125$ ) by a linear function

where the count rate at the end of the observation is 35% lower than that at the beginning. Both the XIS3 (2-s bin) and HXD-PIN (1-s bin) counts are consistent with obeying Poisson distributions, without any significant short-term increases of their count rates.

Figure 2a shows background-subtracted spectra of 4U 0142+61 obtained with three XIS cameras, HXD-PIN, and HXD-GSO. The background levels are also shown. From the HXD-PIN spectrum, we subtracted not only the modeled NXB described in section 2, but also the CXB spectrum taken from Moretti et al. (2009). Although the CXB brightness within the HXD-PIN field of view is expected to vary by  $\sim \pm 12\%$  from sky to sky (Fukazawa et al. 2009), the effect is of the order of 0.5% of the NXB, and hence is negligible compared to the NXB modeling uncertainty. The CXB contribution itself is negligible in the HXD-GSO data.

As seen in figure 2a, the HXD-PIN signals (after removing the NXB and CXB) are statistically significant over the entire 10–70 keV band, and stay  $\gtrsim 10\%$  of the NXB level therein. Since the NXB can be reproduced typically down to  $\lesssim 2\%$  (Fukazawa et al. 2009), the HXD-PIN detection is highly significant with  $\gtrsim 3\sigma$  even considering the systematic errors. In fact, this NXB modeling uncertainty is considerably smaller than the statistical errors. In contrast, the NXB-subtracted HXD-GSO signals are found at a level of  $\sim 1\%$  of the NXB which is a typical systematic uncertainty. Therefore, the source detection with HXD-GSO is considered insignificant only from the spectrum.

In order to grasp basic properties of the spectra of 4U 0142+61 in a model independent way, we normalized them to those of the Crab Nebula (a power-law with a photon index  $\Gamma = 2.1$ ). We utilize the HXD data of the Crab Nebula obtained on 2007 March 20, while employ the simulated Crab Nebula spectrum for the XIS, in order to avoid pile-up effects at the source centroid. The derived ‘‘Crab ratio’’ is presented in figure 1b. Thus, in addition to the long-known soft component, the hard component (section 1) is very clearly visible, rising up from  $\sim 10$  keV and reaching 10 mCrab at 100 keV.

### 3.3. Source pulsations

After applying barycentric corrections to the arrival times of individual photons (Terada et al. 2008), we searched the background-inclusive XIS and HXD data for the 8.7-s source pulsation via standard periodogram analyses. Since the spacecraft wobbling is insignificant on the relevant time scales, the data from XIS0 and XIS1 were also incorporated.

Figure 3 show periodograms obtained with the XIS and HXD-PIN in the 0.8–10 keV and 12–40 keV energy range, respectively. Thus, the pulsation has been detected clearly by the XIS, at a barycentric period of

$$P = 8.68878 \pm 0.00005 \text{ s.} \tag{1}$$

This agrees, within 11  $\mu\text{s}$ , with a value extrapolated from previously measured  $P$  and the period change of  $\dot{P} = 1.960 \times 10^{-12} \text{ s s}^{-1}$  (Gavriil & Kaspi 2002). The width of the XIS periodogram peak is  $\sim 3 \times 10^{-4} \text{ s}$ , or  $\sim 4 \times 10^{-5} P$ . This is consistent with the gross time span of our observation,

$\sim 2.0 \times 10^5$  s (section 2), wherein  $\sim 3 \times 10^4$  pulses are contained.

In the 12–40 keV HXD-PIN periodogram, a peak with  $\chi^2/\nu = 35.9/15 = 2.4$  is found at a consistent period. This gives a chance probability of  $8.4 \times 10^{-4}$  for the HXD-PIN profile to be caused by Poisson fluctuations. An independent and bin-free  $Z_n^2$ -test (Buccheri et al. 1993; Brazier 1994), together with a widely used choice of  $n = 2$ , gives  $Z_n^2 = 21.8$  for the HXD data at the period of (1), with a chance probability of  $2.1 \times 10^{-4}$ . These tests reveal that the HXD-PIN signals are pulsed, at the period of equation 1, with a high significance ( $>99.9\%$ ), even though this level would not be high enough to support the detection of a periodicity without the aid of the XIS data.

Figure 4 shows pulse profiles in the 0.8–4.0, 4.0–10, 10–70, and 80–150 keV energy ranges observed the XIS (XIS0, XIS1, and XIS3), HXD-PIN, and HXD-GSO data, all folded at the period of equation (1), employing an epoch of 54326.356 (MJD). Thus, the pulsation is less significant in the 80–150 keV HXD-GSO data, with  $\chi^2/\nu = 12.2/6 = 2.0$  (null hypothesis probability 0.06). The pulse profiles exhibit some energy-dependent changes, in agreement with previous reports (Kuiper et al. 2006; den Hartog et al. 2008). The peak-to-bottom pulsed fraction,  $(F_{\max} - F_{\min})/(F_{\max} + F_{\min})$ , where  $F_{\max}$  and  $F_{\min}$  are the maximum and minimum background-subtracted count rates across the pulse phase, are evaluated to be  $8.4 \pm 0.3\%$ ,  $13 \pm 1\%$ , and  $\sim 41\%$  in the 0.8–4, 4–10, and 10–70 keV energy ranges, respectively.

### 3.4. Short-Term Variations

Further periodogram analyses of the HXD-PIN data gave an indication that the pulsations in the 12–40 keV band become more prominent toward the latter part of the observation. We hence divided all the exposure into three epochs of  $\sim 30$  ks each, and produced three sets of 12–40 keV HXD-PIN light curves folded at the period of equation (1). As shown in figure 5, the pulse profiles from the 1st and 2nd epochs were found to be consistent with each other within statistical errors. In contrast, as shown in panels (a) and (c) of figure 5, those from the 1st and last epochs appear considerably different; the pulses became deeper and more double-peaked in the 3rd epoch, while the average intensity decreased in agreement with figure 1.1 These effects are unlikely to be caused artificially by cumulative phase errors, which is estimated to be  $<9\%$  of a cycle when folded at equation (1).

To quantitatively examine the suggested pulse-profile changes, we took phase-by-phase differences between the 1st and 3rd epoch pulse profiles, and obtained  $\chi^2 = 20.8$  for  $\nu = 9$ . The calculation took into account (in quadrature) the typical systematic background uncertainty by  $0.004 \text{ c s}^{-1}$  (1 sigma). Since the implied null-hypothesis probability is 1.3%, the two folded profiles are inferred to be different at a 98% confidence level. This suggests that the 12–40 keV signals changed, either in the average intensity or in the pulse profiles (or both). However, these alternative possibilities cannot be distinguished, since the significance of the profile difference reduces to  $\chi^2 = 15.3$  for  $\nu = 9$  (or a chance probability of 8%) if the difference profile is fitted

by a constant.

For reference, the XIS pulse profiles in 0.4-4 keV did not change by more than 7% among the 3 epochs. Any spectral change in the XIS or HXD-PIN band was not significant among the 3 epochs, either.

### 3.5. Spectral Analysis

#### 3.5.1. Wide-band spectra

To quantify the spectral soft and hard components simultaneously, we jointly fitted the data from the XIS, HXD-PIN, and HXD-GSO, in the 0.8–10, 12–70 keV, and 50–200 keV ranges, respectively. Although the signal detection with HXD-GSO is not significant, we include the GSO data points with the systematic error properly added, because we can use them at least as upper-limit points. The on-source and corresponding background spectra were prepared as stated in section 3.1. We also incorporated the correction factor for HXD-GSO spectra, which has been introduced to reproduce the Crab spectra by a single power-law (Takahashi et al. 2008).

As figure 2b shows, the XIS and HXD data points happen to define, in a rather clear-cut way, the soft and hard components, respectively. As the simplest attempt, we separately fitted the XIS spectra with an absorbed blackbody model and the HXD one by a power-law model, to find that the latter is successful with  $\Gamma_{\text{h}} = 0.8_{-0.2}^{+0.4}$  (the former is not; see below). As a next attempt, we tried to jointly reproduce the whole data simultaneously by an absorbed blackbody model plus a power-law model, representing the soft and hard components, respectively. The model normalization between the XIS and HXD-PIN was constrained to be 1.18 (Maeda et al. 2008). When the hard power-law photon index is fixed, for simplicity, at the above value of  $\Gamma_{\text{h}} = 0.8$ , this model gave a blackbody temperature of  $kT \sim 0.46$  keV. However, as shown in figure 6c, the fit was unsuccessful with  $\chi^2/\nu = 7326.9/412 = 17.8$ , due to significant residuals from the blackbody model at  $\sim 1.2$  keV and  $\sim 5$  keV. The resultant parameters are shown in table 1 as Model A. When  $\Gamma$  is allowed to be vary, it became very steep ( $\Gamma \sim 3.7$ ) so as to account for the model inaccuracy below  $\sim 10$  keV rather than to reproduce the hard tail.

Trying to improve the fit, we added a second steep power-law, so that the soft component is now expressed by a sum of a blackbody and a power-law (i.e., BB+PL). The obtained best-fit solution is described by a blackbody of  $kT = 0.43$  keV, a steep power-law of  $\Gamma = 4.0$ , and a hard power-law of  $\Gamma_{\text{h}} = 0.1$  (which is now left free), with a three times larger  $N_{\text{H}}$  value than Model A. Systematic errors of  $\Gamma_{\text{h}}$  are estimated to be  $\sim 30\%$  when considering the 2% uncertainty of the PIN-NXB. However, as shown in figure 6d (Model B in table 1), this model was still unsuccessful with  $\chi^2/\nu = 589.9/409 = 1.44$ , mainly due to deviations in the low energy range of the XIS.

By replacing the steep power-law with a second blackbody, and thus representing the soft component by two blackbodies (or 2BB), the fit was significantly improved to  $\chi^2/\nu =$

459.8/409 = 1.12; these results are shown in figure 6e (Model C in table 1). The two blackbody temperatures were obtained as  $kT_1 = 0.34$  keV and  $kT_2 = 0.63$  keV, with their emission radii (assuming circular regions) as 13.2 km and 2.3 km, respectively, when assuming a distance to the source as 3.6 kpc (Durant & van Kerkwijk 2006a). The absorbing column became  $N_{\text{H}} = 6.4 \times 10^{21} \text{ cm}^{-2}$ .

Although the above Model C is approximately successful, the fit still leaves significant residuals. As one of alternative empirical models for the soft component, we employed, after Tiengo et al. (2005) and Enoto et al. (2010c), the Comptonized blackbody model described in Enoto et al. (2010a). As shown in figure 6e and summarized as Model D in table 1, this model gave a better fit;  $\chi^2/\nu = 441.5/410 = 1.08$ , with  $kT = 0.29$  keV, a soft power-law photon index  $\Gamma_s = 3.8$ , and  $\Gamma_h = 0.4$ . The results using this particular model was already reported previously (Enoto et al. 2010c).

In the strong magnetic field as  $\sim 10^{14}$  G, resonant cyclotron scattering of soft X-ray photons becomes more efficient than Thomson scattering. This effect can be expressed by ‘‘Resonant Cyclotron Scattering (RCS)’’ model (Thompson et al. 2002; Lyutikov & Gavriil 2006; Rea et al. 2008), which calculates a blackbody spectrum modified by resonant cyclotron up-scatterings off hot electrons in the neutron star magnetosphere. This model, combined with the hard power-law, has given a still better account of the data over the 0.8–200 keV energy band, with  $\chi^2/\nu = 362.0/409 = 0.88$ . This fit is shown in figure 6a and figure 6f, and in table 1 as Model E. The derived blackbody temperature ( $\sim 0.3$  keV) is similar to that of Model E, while the Compton optical depth, which was left implicit in Model D, became  $\tau \sim 2.0$ . The photon index of the hard power-law became  $\Gamma_h = 0.89_{-0.10}^{+0.11}(\text{stat.})_{-0.10}^{+0.11}(\text{sys.})$ , which is close to the value of  $\Gamma_h \sim 0.80$  obtained using the HXD-PIN data only.

Figure 7 represents the  $\nu F_\nu$  spectra of 4U 0142+61, fitted with the most successful RCS plus power-law model (Model E) described above. The X-ray flux in the 10–70 keV energy band is  $4.4 \times 10^{-11} \text{ erg cm}^{-2} \text{ s}^{-1}$ , while the unabsorbed 1–10 keV flux is  $1.8 \times 10^{-10} \text{ erg cm}^{-2} \text{ s}^{-1}$ . If the hard component extends to 200 keV, its flux in the 10–200 keV band becomes  $1.5 \times 10^{-10} \text{ erg cm}^{-2} \text{ s}^{-1}$ , which is comparable to that of the soft component.

### 3.5.2. Possible local spectral features

At a closer inspection, we still find negative residuals at  $\sim 20$  keV and  $\sim 40$  keV in the HXD-PIN spectrum (figure 2). Since the NXB spectrum of HXD-PIN shows no spectral features at  $\sim 20$  keV, and only a very weak Gd- $K_\alpha$  emission line at  $\sim 42$  keV, the suggested features cannot be instrumental. However, we refrain from further analysis of these features, because their statistical significance is not high enough.

Lastly, we examined the hard power-law for a high-energy cutoff, because the hard-tail component must steepen at some energies, in order for its luminosity not to diverge. For this purpose, we employed Model D, and multiplied its hard power-law with an exponential cutoff factor of the form  $\exp(-E/E_{\text{cut}})$ , where  $E$  is the photon energy and  $E_{\text{cut}}$  is a cutoff parameter.



Then, the data gave a lower limit as  $E_{\text{cut}} > 180$  keV at the 90% confidence limit. The choice of Model D is because it gives (among the successful 3 models) the flattest value of  $\Gamma_{\text{h}}$ , and hence the derived lower limit on  $E_{\text{cut}}$  is considered to be most conservative.

## 4. Discussion

### 4.1. Wide-band spectra of magnetars

Recent X-ray observations of magnetars show that their persistent broad-band spectra are commonly represented by an optically thick soft component of  $kT \sim 0.3$  keV, and a power-law-like hard-tail component which dominates in energies above  $\sim 10$  keV. Besides, it was revealed that the two-component spectrum depends significantly on their characteristic age, in such a way that the hard-tail component becomes weaker (relative to the soft component), yet harder, towards sources with older characteristic ages (Kaspi & Boydstun 2010; Enoto et al. 2010c). When systematically studying such spectral properties, including in particular the evolutionary behavior revealed by Enoto et al. (2010c), 4U 0142+61 is considered to play a particular important role, for the following three reasons.

First, among the magnetars in the evolutionary study by Enoto et al. (2010c), 4U 0142+61 has the oldest characteristic age, 70 kyr, except for 1E 2259+685 of which the hard-tail component is not well constrained. As a result, 4U 0142+61 is currently the oldest magnetar with the well determined hard-tail component, and hence it significantly reinforces the age-correlated spectral evolution of magnetars (Enoto et al. 2010c). Secondly, as a common characteristic of aged magnetars (Enoto et al. 2010c), the two spectral components of 4U 0142+61 are well separated from each other (see figure 2). This, combined with the relatively high X-ray intensity of 4U 0142+61, allows us to better quantify its two spectral components than in other objects of this class. Finally, the extreme flatness ( $\Gamma_{\text{h}} \sim 0.8$ ) of the hard tail of 4U 0142+61, which is again typical of aged magnetars, is expected to provide very strong constraints on the emission mechanism of the magnetar hard X-rays.

### 4.2. Soft X-ray emission of 4U 0142+61

When comparing among the soft X-ray spectral models in § 3.5.1, the blackbody plus soft power-law model (Model B) requires a higher column density of photo-absorption than the other models. This is likely to be an artifact, necessitated by the too steep low-energy rise of the soft power-law. This soft power-law component, in addition, causes an infrared divergence after eliminating the photo-absorption. Further considering the unacceptable reduced chi-square value, this Model B is unlikely to represent the soft component. Although the two-blackbody model (Model C) can give a better fit, the chi-squared value is still somewhat large. In addition, the associated hard-tail shape,  $\Gamma_{\text{h}} \sim 1.5$ , is considerably larger than that obtained with the HXD alone.

In contrast to Model B and Model C which employ an ad-hoc combination of simple

model components, the two more physical models, Model D and Model E, were found to be more successful with reduced chi-square values of 1.08 and 0.88, respectively (table 1). Both models assume a scenario that some seed photons are repeatedly up-scattered by hot electrons in the stellar magnetosphere; the former is empirically defined (Enoto et al. 2010a), while the latter is based on a simplified 1D semi-analytical modeling (Rea et al. 2008). Thus, these successful wide-band fits suggest that the known deviations of the soft component from a simple blackbody can be ascribed, at least partially, to up-scattering of soft seed photons off hot electrons located somewhere. Below, let us discuss a possible scenario, employing the latter modeling (Model E), which is more specific.

As shown in figure 6, Model E has given an acceptable fit to the 0.8–200 keV spectrum, with a seed-photon temperature of  $kT = 0.30$ , an optical depth of  $\tau = 2.0$ , and an electron thermal velocity of  $\beta = 0.3$ . These parameters are consistent with  $kT = 0.30$ ,  $\tau = 1.9$ , and  $\beta = 0.33$ , derived by a combined fitting of the 2004 XMM-Newton observation and 2003-2006 INTEGRAL observations using the same RCS plus a hard tail power-law modeling (Rea et al. 2008). Thus the soft X-ray spectral shape measured in 2007 has little difference from that in 2004. Therefore, the persistent soft X-ray emission of 4U 0142+61 is relatively stable at least on a time scale of a few years. In addition, the absorbing column density measured with Suzaku,  $N_{\text{H}} = 6.72_{-0.04}^{+0.38} \times 10^{21} \text{ cm}^{-2}$ , is in a good agreement with  $N_{\text{H}} = (6.4 \pm 0.7) \times 10^{21} \text{ cm}^2$  derived by absorption edges of elements such as O, Fe, Ne, Mg, and Si (Durant & van Kerkwijk 2006b).

When using Model E, the overall soft-component shape mainly determines the blackbody temperature  $kT$ , while the data excess above the blackbody toward higher energies, to be called “soft tail”, specifies  $\tau$  and  $\beta$ . The derived blackbody temperature,  $kT \sim 0.3 \text{ keV}$ , is similar to those derived by Model C and Model D. (If using a more familiar Comptonized blackbody model, “compbb”, we obtain  $\tau \sim 2.9$ ,  $kT \sim 0.32 \text{ keV}$ , and an electron temperature  $kT_e \sim 2.3 \text{ keV}$ .) Then, let us discuss whether these conditions of Model E are physically realistic in view of general pictures of magnetized neutron stars. These parameters imply that seed photons with  $kT \sim 0.3 \text{ keV}$ , presumably from the stellar surface, pass through a scattering slab with an optical depth of  $\sim 2$ , filled with electrons which have typical velocities of  $0.3c$ , where  $c$  is the speed of light. Since the magnetic field of 4U 0142+61 is estimated as  $B \sim 1.3 \times 10^{14} \text{ G}$  from the period  $P \sim 8.68 \text{ s}$  and its derivative  $\dot{P} \sim 2 \times 10^{-12} \text{ s s}^{-1}$ , the corresponding Goldreich-Julian density (Goldreich & Julian 1969) becomes  $n_{\text{GJ}} = 7 \times 10^{13} (P/1 \text{ s})^{-1} (B/10^{15} \text{ G}) \text{ cm}^{-3} = 1 \times 10^{12} \text{ cm}^{-3}$ . If assuming this density, the Thomson cross-section  $\sigma_{\text{T}}$ , and a slab thickness of  $l \sim 10^7 \text{ cm}$ , the corresponding optical depth becomes  $\tau \sim n_{\text{GJ}} \sigma_{\text{T}} l \sim 7 \times 10^{-6}$ , which is much smaller than the value,  $\tau \sim 2$ , required by the soft-tail feature in the data. However, consideration of more detailed physics of magnetars, as employed in the RCS model, allows us to solve this discrepancy by invoking two effects; a larger electron density and an enhanced electron-photon cross-section. The former is expected under a twisted magnetic configuration, where

electric currents are induced to give  $\sim 3$ – $4$  orders of magnitude higher electron density than  $n_{\text{GJ}}$  (Thompson et al. 2002). The latter, an enhanced cross-section, can occur at a cyclotron resonance energy in the scattering slab (Lyutikov & Gavriil 2006). These larger density and cross-section are consistent with a basic scheme of the magnetar hypothesis.

#### 4.3. *Hard X-ray emission of 4U 0142+61*

The fit with Model E has given the photon index of the hard component as  $\Gamma_{\text{h}} = 0.89_{-0.10}^{+0.11}(\text{stat.})_{-0.10}^{+0.11}(\text{sys.})$ . This is consistent with, and of similar quality to, the value of  $0.93 \pm 0.06$  measured by INTEGRAL (den Hartog et al. 2008), or that based on the XMM-Newton and INTEGRAL data,  $1.1 \pm 0.1$  (Rea et al. 2008), even though the Suzaku exposure,  $\sim 100$  ks, is much shorter than that with INTEGRAL. Among the magnetars shown in figure 4 in Enoto et al. (2010c), 4U 0142+61 thus exhibits one of the hardest power-law components.

The emission mechanism of the hard X-ray component is a topic of extensive discussion. Although several scenarios have been proposed, none of them succeeds to explain all the observational properties. So far, one of the biggest difficulties therein has been how to explain the extremely hard photon indices ( $\Gamma_{\text{h}} \sim 1$  or less; figure 7). Now, the difficulty is enhanced by the systematic change in  $\Gamma_{\text{h}}$  (from  $\sim 1.7$  to  $\sim 0.4$ ) in correlation with the characteristic age (Kaspi & Boydstun 2010; Enoto et al. 2010c). Indeed, this effect cannot be readily explained by the non-thermal radiation model from fast-mode break down (Heyl & Hernquist 2005), or the thermal bremsstrahlung model from a transition layer (Thompson & Beloborodov 2005; Beloborodov & Thompson 2007), or the resonant inverse-Compton up-scattering model (Baring & Harding 2007).

A possible observational hint to the emission mechanism of the hard component may be provided by the highest energies to which the hard tail extends. There is a relatively strong COMPTEL upper limit above  $\gtrsim 750$  keV (Kuiper et al. 2006). In order to make this point clear, we show, in figure 8, a multi-band spectral energy distribution of 4U 0142+61, incorporating previously reported multi-wavelength observations. Thus, if time variations are negligible among these observations, the hard X-ray spectrum must turn over at energies between  $\sim 200$  and  $\sim 750$  keV. The Suzaku lower limit on the cutoff,  $E_{\text{cut}} > 180$  keV, is consistent with the above estimate. If this hard power-law component originates from non-thermal emission from accelerated particles, the cutoff would reflect the maximum particle energy. However, considering the difficulty with the ordinary non-thermal emission processes by energetic particles to explain the values of  $\Gamma_{\text{h}}$  and its systematic source-to-source differences, the cutoff may alternatively be interpreted as an effect of the extremely high magnetic field, typically exceeding the critical field  $B_{\text{cr}} = 4.41 \times 10^{13}$  G, where gamma-rays cannot directly escape due to photon splitting (Harding & Lai 2006).

This photon-splitting view implies a possibility of the hard X-ray emission arising via down-cascade of energetic gamma-rays (Harding et al. 1997; Enoto et al. 2010d). Near the

stellar surface, gamma-rays above a few hundred keV can be produced through, e.g., resonant cyclotron scattering, annihilation of electron-positron pairs at the dense stellar atmosphere, and sporadic reconnection. In ultra-strong magnetic fields exceeding  $B_{\text{cr}}$ , electron-positron pair cascades are suppressed (Baring & Harding 2001), while the photon splitting may be dominant (Baring & Harding 2001; Harding & Lai 2006). As a result, these gamma-rays from the surface may repeatedly split into lower energy photons, since the photon splitting process has no low-energy threshold unlike the one-photon pair production process. In fact, Harding et al. (1997) reported that the photon splitting becomes important at  $B \gtrsim 0.3B_{\text{cr}}$ , since the attenuation length due to splitting become comparable to or less than those for pair production. This process can also explain the differences in  $\Gamma_{\text{h}}$  among magnetars, in such a way that higher fields of younger objects will allow the photon-splitting cascade to proceed down to lower energies, and hence to make the continuum softer.

#### 4.4. Energetics

Assuming an isotropic emission at an distance of 3.6 kpc (Durant & van Kerkwijk 2006a), the soft (RCS) and hard components are implied to have unabsorbed luminosities of  $2.8 \times 10^{35}$  erg s<sup>-1</sup> and  $6.8 \times 10^{34}$  erg s<sup>-1</sup>, in the 1–10 keV and 10–70 keV band, respectively. If calculated in the 2–10 keV band, our soft-component luminosity becomes  $1.1 \times 10^{35}$  erg s<sup>-1</sup>. Since this agrees with the previous measurements (Durant & van Kerkwijk 2006a), the soft component is inferred to be stable, making some theoretical prediction (Thompson & Duncan 1996) consistent with the observation. Adding up the soft and hard components, the absorption-corrected 1-200 keV luminosity becomes  $5.2 \times 10^{35}$  erg s<sup>-1</sup>, which can be decomposed into  $\sim 54\%$  and  $\sim 46\%$  carried by the soft and hard components, respectively. Since the spin-down luminosity of the source is only  $1.2 \times 10^{32}$  erg s<sup>-1</sup>, neither components can be powered by the rotational energy.

#### 4.5. Pulse profiles

The soft and hard X-ray pulse profiles, obtained with Suzaku (figure 4), are generally consistent with those measured previously with INTEGRAL and RXTE (Kuiper et al. 2006; den Hartog et al. 2008). In energies below a few keV, the profile has two peaks, and one of them (phase at  $\sim 0.5$  in our figure 4 and  $0.1$  in figure 5 of Kuiper et al. 2006) becomes weaker towards 10 keV, but it partially recovers towards a few tens keV at a somewhat smaller pulse phase.

As seen above, the pulse profiles of 4U 0142+61 depend in a complex way on the energy. However, the main peaks of the two spectral components are at the same phase  $\sim 1$  in figure 4, and their emission regions seem to be located at the same rotation phase. Regarding the soft component as an optically-thick thermal emission from the polar-cap regions of the neutron star, we further speculate that the spectral hard-tail component, which are generally pulsed strongly (e.g., Kuiper et al. 2006), is also emitted from the polar-cap regions. This inference gives an additional support to the photon-splitting mechanism, because the input gamma-rays will be produced, e.g., via electron-positron annihilation, mainly at the polar-cap regions.

In subsection 3.4 and figure 5, we presented evidence for short-term (in 30 ks) variations in the pulse profile (or overall signal intensity). During the last 30 ks of our exposure, when the hard X-ray intensity slightly decreased (figure 1), the HXD-PIN pulse profile possibly became more strongly pulsed and more double peaked. These effects, if real, may reflect some sporadic processes involved in the hard-tail production mechanism. For example, if the persistent emission of a magnetar is formed by an assembly of numerous small short bursts (Nakagawa et al. 2007), the persistent intensity should fluctuate due to statistical fluctuations of the number of small bursts. We expect the soft spectral component to be more stable, because of the heat capacity of the neutron star. More quantitative evaluation of these issues will be presented elsewhere.

## 5. Conclusion

We observed the prototypical anomalous X-ray pulsar 4U 0142+61 with Suzaku, and quantified its wide-band spectra, spanning from 0.4 to  $\sim 70$  keV or higher (subsection 3.2). This is a first detailed broad-band study of this source performed using a single satellite within a short exposure ( $\sim 100$  ks), without cross-calibration uncertainties among multiple satellites. We reconfirmed the hard-tail component above 10 keV, with high significance of  $\gtrsim 3\sigma$ . Detailed analyses of the soft and hard X-ray spectra, simultaneously fitted by several spectral models (subsection 3.5.1), shows that the soft component is represented by Comptonized blackbody model or Resonant Cyclotron Scattering model with a seed-photon temperature of  $kT \sim 0.3$  keV. The hard-tail component can be fitted by a power-law with a photon index of  $\Gamma_h \sim 0.9$ , together with a constraint on its cutoff as  $E_{\text{cut}} > 180$  keV. The folded pulse profiles in the 12–40 keV range exhibited evidence for shape or intensity variations on a time scale of 30 ks (subsection 3.4), suggesting some sporadic process in the hard X-ray production process. We propose the photon splitting process as a promising production mechanism for the hard X-ray component.

We are grateful to all the Suzaku team members, including in particular M. Morii for his elucidating discussion.

## References

- The Fermi-LAT collaboration 2010, arXiv:1011.0091  
 Baring, M. G., & Harding, A. K. 2001, ApJ, 547, 929  
 Baring, M. G., & Harding, A. K. 2007, Ap&SS, 308, 109  
 Beloborodov, A. M., & Thompson, C. 2007, ApJ, 657, 967  
 Buccheri, R., et al. 1993, Advances in Space Research, 13, 727  
 Brazier, K. T. S. 1994, MNRAS, 268, 709  
 den Hartog, P. R., Hermsen, W., Kuiper, L., Vink, J., in't Zand, J. J. M., & Collmar, W. 2006, A&A,

451, 587

- den Hartog, P. R., Kuiper, L., Hermsen, W., Rea, N., Durant, M., Stappers, B., Kaspi, V. M., & Dib, R. 2007, *Ap&SS*, 308, 647
- den Hartog, P. R., Kuiper, L., Hermsen, W., Kaspi, V. M., Dib, R., Knödlseeder, J., & Gavriil, F. P. 2008, *A&A*, 489, 245
- Duncan, R. C., & Thompson, C. 1992, *ApJL*, 392, L9
- Durant, M., & van Kerkwijk, M. H. 2006, *ApJ*, 650, 1070
- Durant, M., & van Kerkwijk, M. H. 2006, *ApJ*, 650, 1082
- Durant, M., & van Kerkwijk, M. H. 2006, *ApJ*, 652, 576
- Enoto, T., et al. 2009, *ApJL*, 693, L122
- Enoto, T., et al. 2010a, *PASJ*, 62, 475
- Enoto, T., et al. 2010b, *ApJ*, 715, 665
- Enoto, T., et al. 2010c, *ApJL*, 722, L162
- Enoto, T., et al. 2010d, Ph.D thesis, The University of Tokyo
- Fukazawa, Y., et al. 2009, *PASJ*, 61, 17
- Gaensler, B. M., Slane, P. O., Gotthelf, E. V., & Vasisht, G. 2001, *ApJ*, 559, 963
- Gavriil, F. P., & Kaspi, V. M. 2002, *ApJ*, 567, 1067
- Gogus, E., Woods, P. M., Kouveliotou, C., Kaneko, Y., Gaensler, B. M., & Chatterjee, S. 2010, arXiv:1008.4089
- Goldreich, P., & Julian, W. H. 1969, *ApJ*, 157, 869
- Götz, D., Mereghetti, S., & Hurley, K. 2007, *Ap&SS*, 308, 51
- Halpern, J. P., Gotthelf, E. V., Reynolds, J., Ransom, S. M., & Camilo, F. 2008, *ApJ*, 676, 1178
- Harding, A. K., Baring, M. G., & Gonthier, P. L. 1997, *ApJ*, 476, 246
- Harding, A. K., & Lai, D. 2006, *Reports on Progress in Physics*, 69, 2631
- Heyl, J. S., & Hernquist, L. 2005, *ApJ*, 618, 463
- Heyl, J. S., & Hernquist, L. 2005, *MNRAS*, 362, 777
- Hulleman, F., van Kerkwijk, M. H., & Kulkarni, S. R. 2004, *A&A*, 416, 1037
- Ishisaki, Y., et al. 2007, *PASJ*, 59, 113
- Israel, G. L., Mereghetti, S., & Stella, L. 1994, *ApJL*, 433, L25
- Kaspi, V. M., & Boydston, K. 2010, *ApJL*, 710, L115
- Kokubun, M., et al. 2007, *PASJ*, 59, 53
- Koyama, K., et al. 2007, *PASJ*, 59, 23
- Kuiper, L., Hermsen, W., den Hartog, P. R., & Collmar, W. 2006, *ApJ*, 645, 556
- Kuiper, L., Hermsen, W., & Mendez, M. 2004, *ApJ*, 613, 1173
- Lyutikov, M., & Gavriil, F. P. 2006, *MNRAS*, 368, 690
- Maeda, Y., Someya, K., & Ishida, M. 2008, JX-ISAS-SUZAKU-MEMO-2008-06
- Mitsuda, K., et al. 2007, *PASJ*, 59, 1
- Mereghetti, S., Götz, D., Mirabel, I. F., & Hurley, K. 2005, *A&A*, 433, L9
- Moretti, A., et al. 2009, *A&A*, 493, 501
- Nakagawa 2007, Ph.D. Thesis, Aoyama Gakuin University
- Nakagawa, Y. E., et al. 2007, *PASJ*, 59, 653

Uchiyama, Y., et al. 2008, PASJ, 60, 35  
Rea, N., et al. 2007, MNRAS, 381, 293  
Rea, N., Zane, S., Turolla, R., Lyutikov, M., & Gotz, D. 2008, ArXiv e-prints, 802, arXiv:0802.1923  
Rea, N., et al. 2009, MNRAS, 396, 2419  
Takahashi, T., et al. 2007, PASJ, 59, 35  
Takahashi, H., et al. 2008, PASJ, 60, 69  
Terada, Y., et al. 2008, PASJ, 60, 25  
Tiengo, A., Mereghetti, S., Turolla, R., Zane, S., Rea, N., Stella, L., & Israel, G. L. 2005, A&A, 437, 997  
Thompson, C., & Duncan, R. C. 1995, MNRAS, 275, 255  
Thompson, C., & Duncan, R. C. 1996, ApJ, 473, 322  
Thompson, C., et al. 2002, ApJ, 574, 332  
Thompson, C., & Beloborodov, A. M. 2005, ApJ, 634, 565  
Uchiyama, Y., et al. 2008, PASJ, 60, 35  
Wang, Z., Chakrabarty, D., & Kaplan, D. L. 2006, Nature, 440, 772  
Woods, P. M., & Thompson, C. 2006, Compact stellar X-ray sources, 547

**Table 1.** Spectral parameters of 4U 0142+61 observed in 2007 August\*.

	Model A	Model B	Model C	Model D	Model E
	BB+hPL	BB+sPL+hPL	2BB+hPL	CBB+hPL	RCS+hPL
Absorbed soft flux <sup>†</sup>	66.0	64.7 ± 0.2	64.4 ± 0.6	64.4 ± 0.2	64.4 <sup>+7.0</sup> <sub>-6.4</sub>
Absorbed hard flux <sup>‡</sup>	83.2	34.6 <sup>+3.7</sup> <sub>-4.0</sub>	21.7 <sup>+3.0</sup> <sub>-3.8</sub>	37.2 <sup>+3.5</sup> <sub>-3.7</sub>	32.8 <sup>+3.2</sup> <sub>-2.9</sub>
$N_{\text{H}}$ ( $10^{22}$ cm <sup>2</sup> )	0.40	1.12 ± 0.02	0.64 ± 0.01	0.63 ± 0.01	0.672 <sup>+0.038</sup> <sub>-0.004</sub>
$kT_1$ (keV)	–	–	0.337 <sup>+0.006</sup> <sub>-0.007</sub>	–	–
$R_1$ (km) <sup>§</sup>	–	–	13.2 <sup>+0.6</sup> <sub>-0.5</sub>	–	–
$kT_2$ (keV)	–	–	0.63 ± 0.02	–	–
$R_2$ (km) <sup>§</sup>	–	–	2.3 <sup>+0.3</sup> <sub>-0.2</sub>	–	–
$kT$	0.46	0.428 ± 0.004	–	0.289 <sup>+0.003</sup> <sub>-0.002</sub>	0.30 <sup>+0.03</sup> <sub>-0.12</sub>
$\Gamma_{\text{soft}}$	–	3.95 <sup>+0.04</sup> <sub>-0.03</sub>	–	–	–
$\alpha$ ( $=\Gamma_{\text{S}} - 1$ ) <sup>  </sup>	–	–	–	3.78 <sup>+0.04</sup> <sub>-0.03</sub>	–
RCS $\tau$	–	–	–	–	1.98 <sup>+0.07</sup> <sub>-0.06</sub>
RCS $\beta$	–	–	–	–	0.32 <sup>+0.01</sup> <sub>-0.02</sub>
$\Gamma_{\text{h}}$	0.80 (fix)	0.11 <sup>+0.13</sup> <sub>-0.11</sub>	1.54 ± 0.13	0.40 <sup>+0.11</sup> <sub>-0.09</sub>	0.89 <sup>+0.11</sup> <sub>-0.10</sub>
$\chi^2/\text{d.o.f}$	7326.9/412	589.9/409	459.8/409	441.5/410	362.0/409
$\chi^2_{\nu}$	17.8	1.44	1.12	1.08	0.88
Probability	$< 10^{-5}$	$1 \times 10^{-8}$	0.042	0.14	0.95

\* BB, PL, CBB and RCS represent blackbody, power-law, (magnetic) comptonized blackbody, and resonant cyclotron scattering, respectively. All the quoted errors are only statistical at the 90% confidence level.

Lower-case characters “h” and “s” in model names represent “hard” and “soft”, respectively.

<sup>†</sup> The absorbed X-ray fluxes ( $10^{-12}$  ergs s<sup>-1</sup> cm<sup>-2</sup>) in the 2–10 keV.

<sup>‡</sup> The X-ray flux ( $10^{-12}$  ergs s<sup>-1</sup> cm<sup>-2</sup>) in the 15–60 keV.

<sup>§</sup> Distance to 4U 0142+61 is assumed at 3.6 kpc.

<sup>||</sup> The parameter  $\alpha$  is related with the soft tail power-law as  $\alpha = \Gamma_{\text{s}} - 1$ , and describes Comptonization process. Details are given in an appendix of Enoto et al. (2010a).



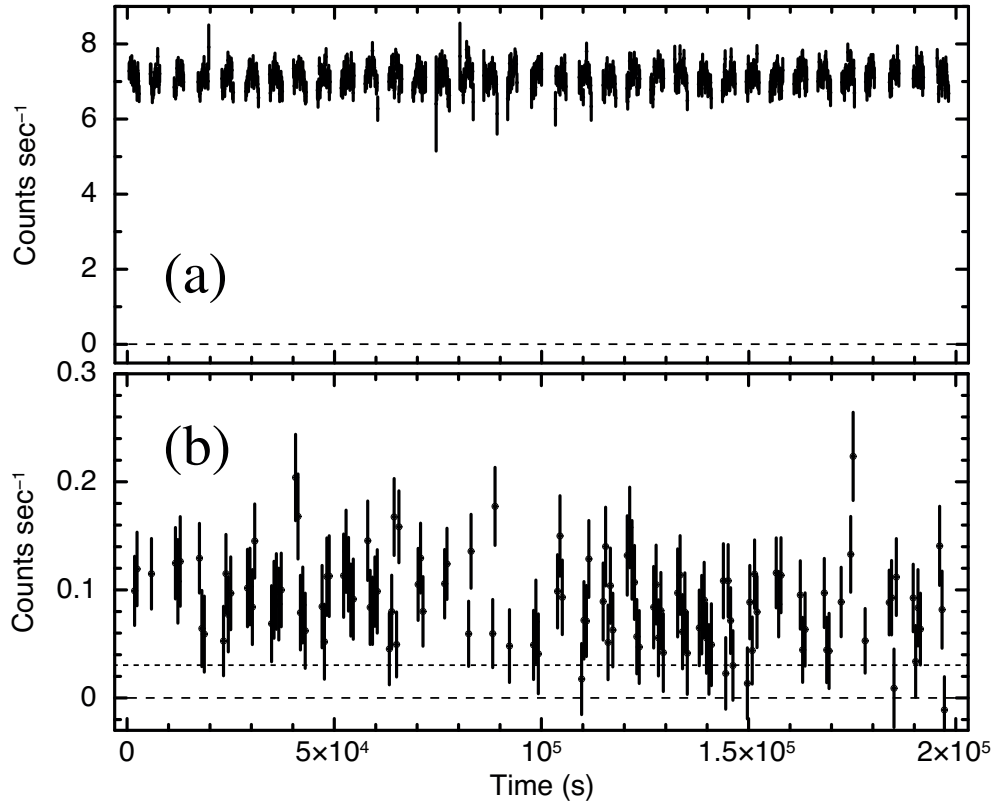


**Fig. 1.** (a) Background-subtracted 0.4–10 keV light curve of XIS3, with a binning of 160 s. (b) The NXB-subtracted HXD-PIN light curve in the 10–70 keV range, with 550 s binning. It still includes the CXB contribution by  $\sim 0.03 \text{ c s}^{-1}$ , which is shown as a dotted line.

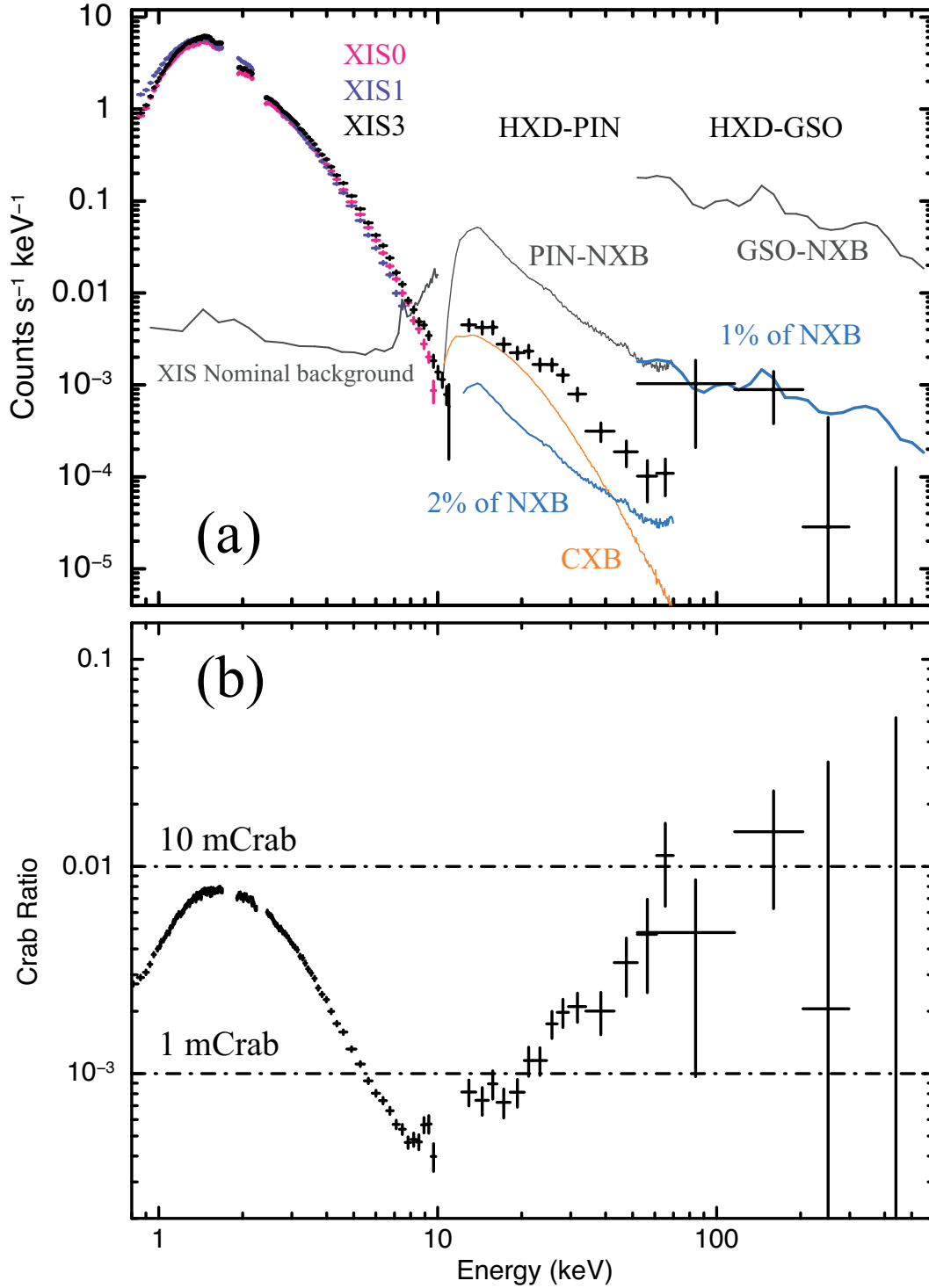


**Fig. 2.** (a) Background-subtracted Suzaku spectra of 4U 0142+61 obtained with the XIS, HXD-PIN, and HXD-GSO. Not only the NXB but also the CXB contribution was subtracted from the HXD-PIN data. The error bars are statistical only for the XIS and HXD-PIN, while those of HXD-GSO include systematic errors as well. (b) The same spectra as presented in panel (a), but divided by those of the Crab Nebula.

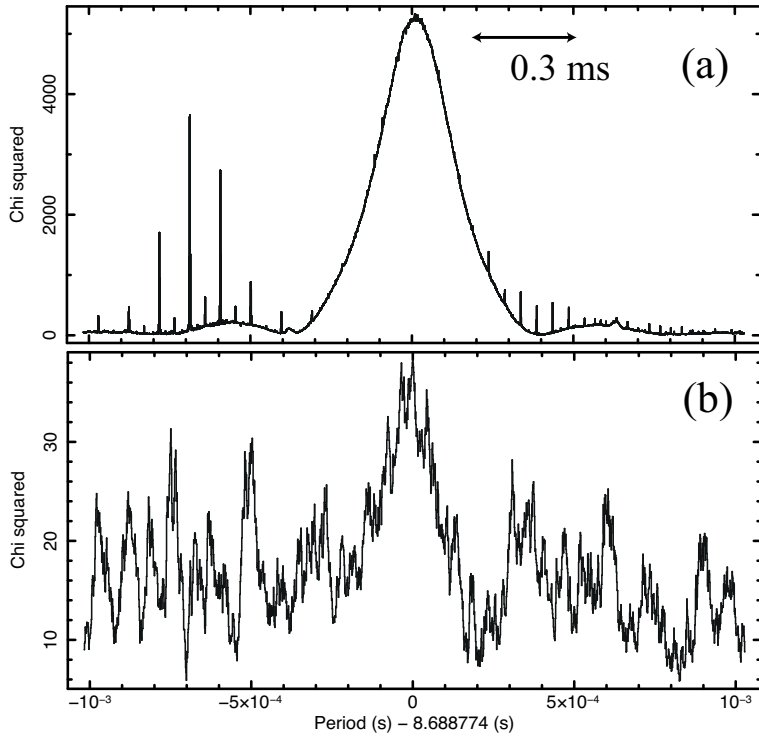


**Fig. 3.** Periodograms from XIS0+XIS1+XIS3 (panel a: 0.8–10 keV) and HXD-PIN (panel b: 12–40 keV), calculated using 0.54 s binned light curves and 16 bins for one pulse period. The backgrounds are inclusive.

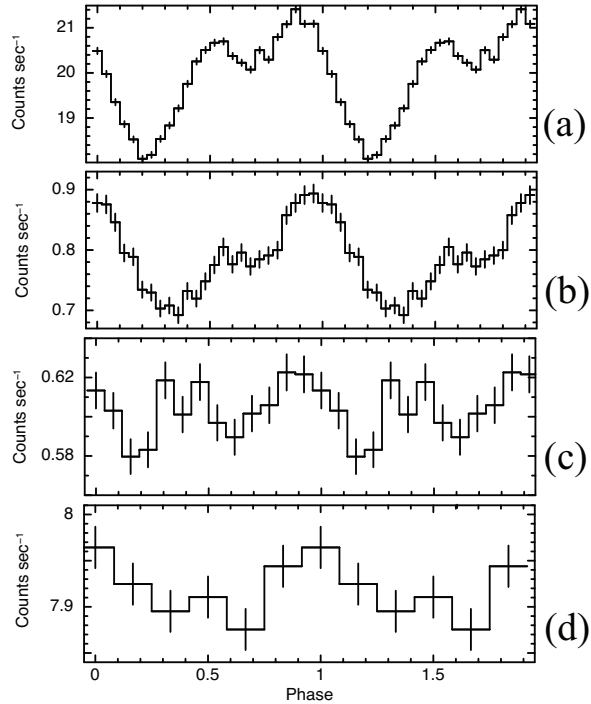


**Fig. 4.** Background-inclusive XIS (XIS0, XIS1, and XIS3 summed), HXD-PIN, and HXD-GSO pulse profiles, obtained by folding the total data at the pulse period of equation (1), in (a) 0.8–4.0, (b) 4.0–10, (c) 10–70, and (d) 80–150 keV ranges. The HXD data is corrected for the dead time. Corresponding background rates are estimated to be  $(1.34 \pm 0.04) \times 10^{-1}$  counts  $\text{sec}^{-1}$ ,  $(1.94 \pm 0.14) \times 10^{-2}$  counts  $\text{sec}^{-1}$ ,  $(5.49 \pm 0.11) \times 10^{-1}$  counts  $\text{sec}^{-1}$ , and  $5.00 \pm 0.21$  counts  $\text{sec}^{-1}$ , for panels (a), (b), (c), and (d), respectively. These background rates include only statistical errors for the XIS and both statistical and systematic errors for the HXD. We assumed 2% and 0.6% systematic errors for the PIN-NXB and the GSO-NXB, respectively.

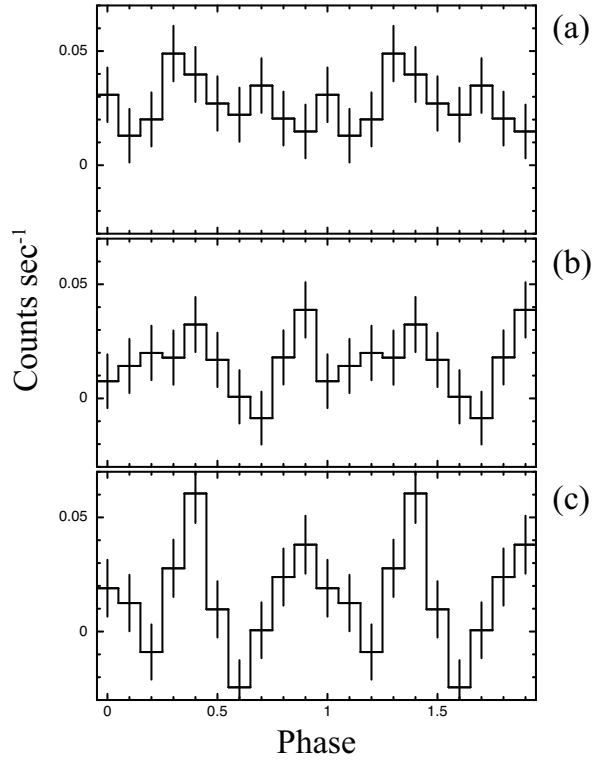


**Fig. 5.** NXB- and CXB- subtracted and deadtime-corrected 12–40 keV HXD-PIN pulse profiles, during (a) 1st, (b) 2nd, and (c) 3rd 30 ks intervals, respectively. Error bars are statistical ( $1\sigma$ ) only, whereas the systematic errors of the background subtraction is  $\sim 0.004 \text{ c s}^{-1}$ .

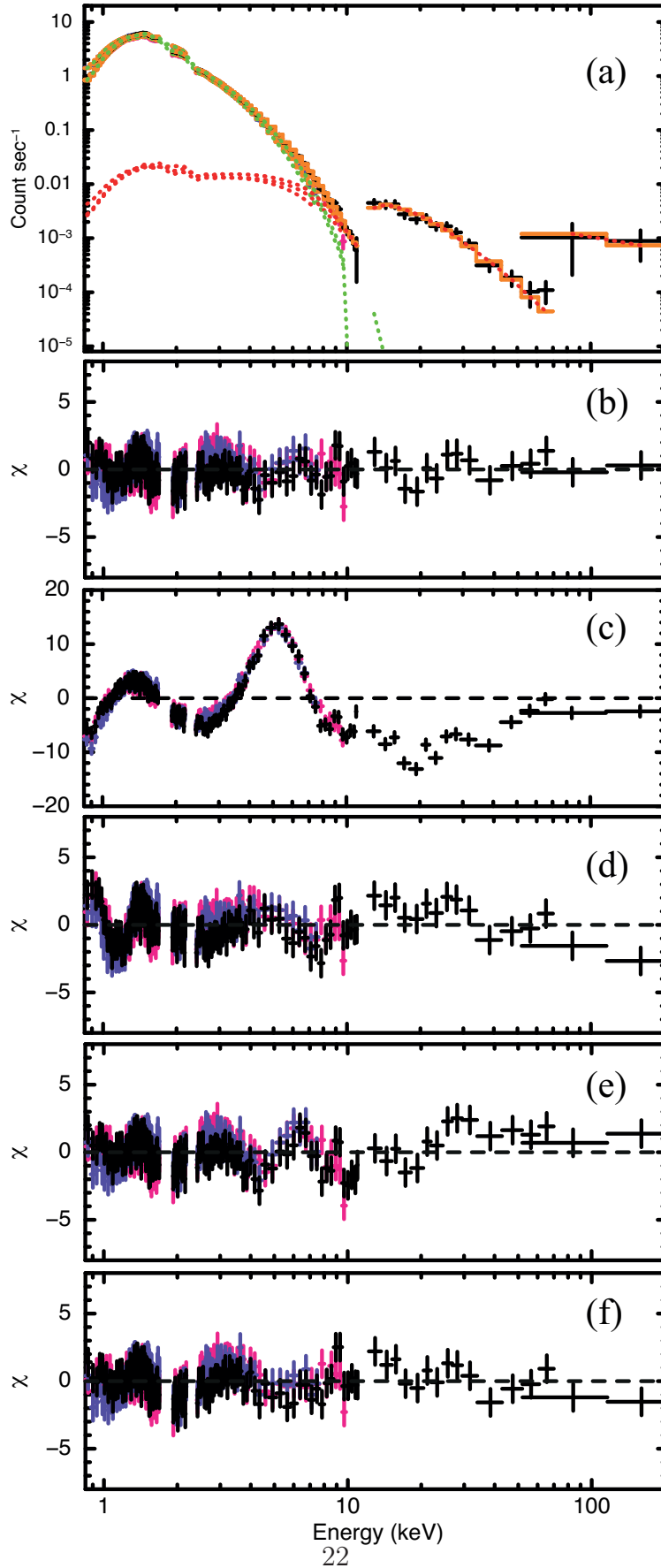


**Fig. 6.** (a) The same Suzaku spectra of 4U 0142+61 as shown in figure 2, fitted by RCS (green)+PL (magenta) model, namely Model E. (b) Residuals from the fit in panel (a). (c)(d)(e)(f) The same as panel (b), but the soft component is represented by BB (Model A), BB+PL (Model B), 2BB (Model C), and CBB (Model D) models, respectively.

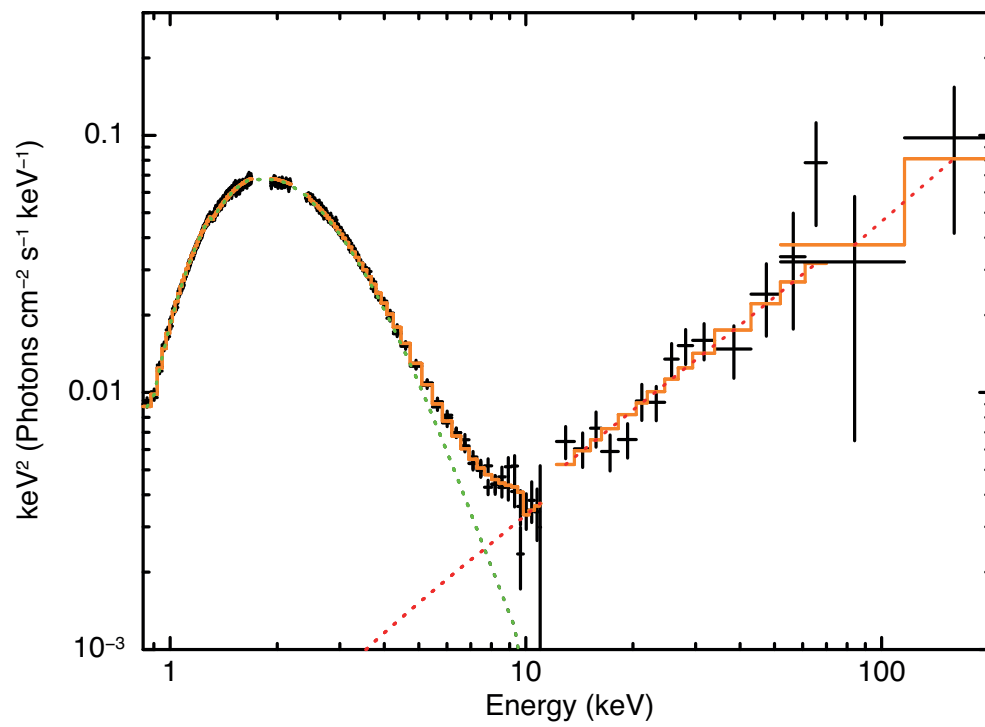
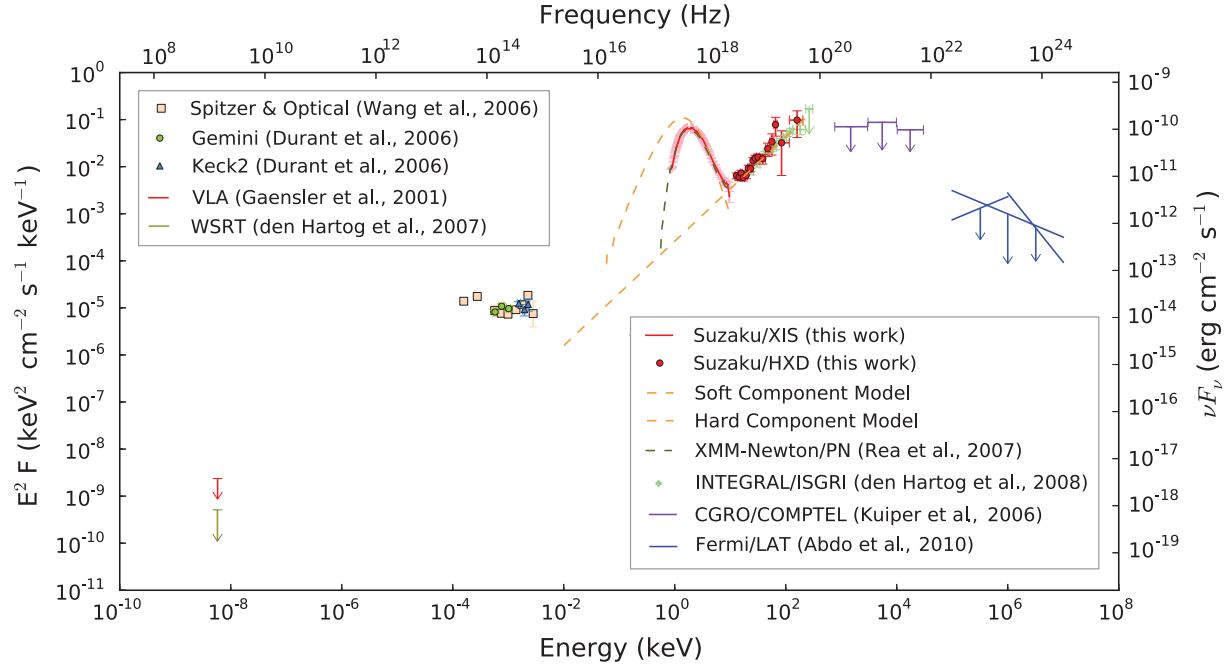


Fig. 7. The same results as in figure 6a but shown in the decomvolved  $\nu F_\nu$  form.



**Fig. 8.** A multi-band spectral energy distribution of 4U 0142+61. The Suzaku data are shown in the 0.8–10 keV and 12–200 keV energy ranges from the XIS and the HXD, respectively. The soft and hard components of Model E are represented by dashed lines after corrections for the interstellar absorption, and are extrapolated to lower energies. The previous X-ray results are also shown; the 0.1–200 keV band from the XMM-Newton/PN (Rea et al. 2007; Abdo et al. 2010) and the INTEGRAL/ISGRI data sets (den Hartog et al. 2008). In the gamma-ray energy band, the  $2\sigma$  CGRO/COMPTEL upper limits (den Hartog et al. 2006; Kuiper et al. 2006) and 95% Fermi/LAT upper limits (Abdo et al. 2010) are plotted. In the infrared and optical ranges, Spitzer observations at  $4.5 \mu\text{m}$  and  $8.0 \mu\text{m}$  (Wang et al. 2006) and some data sets from Gemini and Keck II (Durant & van Kerkwijk 2006c; Hulleman et al. 2004) are shown, where the optical data are de-extincted assuming a reddening value of  $A_V = 3.5$ . In the radio band, a  $2\sigma$  upper limit from 1.38 GHz WSRT continuum (den Hartog et al. 2007), and the 1.4 GHz VLA upper limit (Gaensler et al. 2001) are shown.